

PCCP

Accepted Manuscript

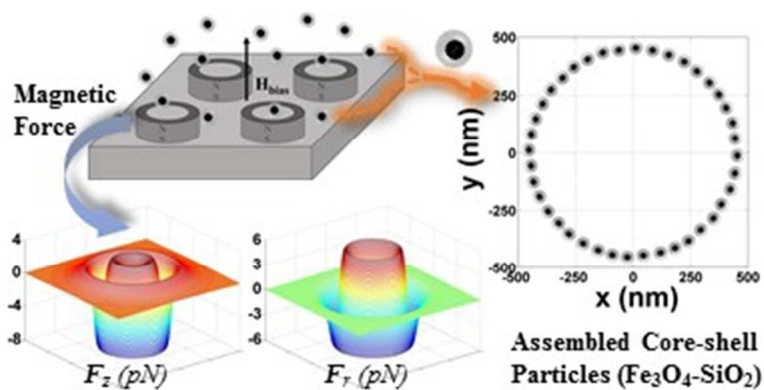


This is an *Accepted Manuscript*, which has been through the Royal Society of Chemistry peer review process and has been accepted for publication.

Accepted Manuscripts are published online shortly after acceptance, before technical editing, formatting and proof reading. Using this free service, authors can make their results available to the community, in citable form, before we publish the edited article. We will replace this *Accepted Manuscript* with the edited and formatted *Advance Article* as soon as it is available.

You can find more information about *Accepted Manuscripts* in the [Information for Authors](#).

Please note that technical editing may introduce minor changes to the text and/or graphics, which may alter content. The journal's standard [Terms & Conditions](#) and the [Ethical guidelines](#) still apply. In no event shall the Royal Society of Chemistry be held responsible for any errors or omissions in this *Accepted Manuscript* or any consequences arising from the use of any information it contains.



Controlling the assembly of colloidal magnetic core-shell particles into patterned monolayer structures with nanoscale feature resolution using soft-magnetic template elements
80x40mm (120 x 120 DPI)

Template-assisted Nano-patterning of Magnetic Core-shell Particles in Gradient Fields

Cite this: DOI: 10.1039/x0xx00000x

Xiaozheng Xue^a and Edward P. Furlani^{a,b},

Received 00th January 2012,
Accepted 00th January 2012

DOI: 10.1039/x0xx00000x

www.rsc.org/

A method is proposed for controlling the assembly of colloidal magnetic core-shell nanoparticles into patterned monolayer structures with nanoscale feature resolution. The method is based on magnetic field-directed self-assembly that is enhanced using soft-magnetic template elements. The elements are embedded in a nonmagnetic substrate and magnetized using a uniform bias field. A key feature of this approach is the combined use of a uniform field with induced gradient-fields produced by the template elements. This enables the customization of a force field with localized regions of attractive and repulsive magnetic force that provide extraordinary control of particle motion during assembly. The method is demonstrated using a computational model that simulates the assembly process taking into magnetic and hydrodynamic forces including interparticle interactions, Brownian diffusion, Van der Waals force and effects of surfactants. The analysis shows that extended geometric patterns of particles can be assembled with nanoscale resolution, beyond that of the template elements, within milliseconds. This is achieved by tailoring key parameters including the template geometry to produce a force field that focuses the particles into prescribed patterns; the thickness of the dielectric particle shell to control the magnetic dipole-dipole force upon contact and the particle volume fraction to suppress undesired aggregation during assembly. The proposed method broadly applies to arbitrary template geometries and multi-layered core-shell particles with at least one magnetic component. It can enable the self-assembly of complex patterns of nanoparticles and open up opportunities for the scalable fabrication of multifunctional nanostructured materials for a broad range of applications.

Keywords: Field-directed assembly of core-shell nanoparticles, template-assisted self-assembly of magnetic-dielectric core-shell nanoparticles, magnetic dipole-dipole interactions.

1 Introduction

The interest in the field-directed manipulation of colloidal magnetic particles has grown dramatically over the years due to rapid advances in particle synthesis and related enabling technologies¹⁻⁴, there has been a corresponding proliferation of applications spanning a range of fields that include drug delivery^{5,6}, gene transfection^{7,8,9}, microfluidic-based bioseparation¹⁰ and sorting¹¹, micro-mixing and bio-chemical sensing. More generally, there has been ongoing emphasis on the development methods for controlling the self-assembly of colloidal particles of all kinds into extended patterned structures. The motivation for this work comes in part from a desire for a bottom-up approach for the scalable fabrication of integrated nanostructured materials, e.g. for photonic^{12,13}, magnetic, micro-optical¹⁴ and electronic^{15,16} applications. Such an approach would provide advantages over conventional top-down lithographic-based fabrication and would open up opportunities for the low-cost high-throughput production of functional nanostructured materials. Various methods have

been demonstrated for the assembly of single¹⁷⁻²² and multiple component^{23,24} colloids into extended patterns. Some methods rely on directed^{23,25} or template-assisted²⁶ assembly or combinations thereof. However, despite this progress, the assembly of patterned structures with nanoscale feature resolution still remains very challenging. The focus of this work is on a method for achieving this using magnetic-dielectric core-shell nanoparticle colloids.

In this paper we propose a method for controlling the directed assembly of colloidal magnetic-dielectric core-shell nanoparticles into extended monolayer patterns with nanoscale resolution. The method is based on magnetic field-directed self-assembly that is enhanced using soft-magnetic template elements. The elements are embedded in a nonmagnetic substrate and magnetized using a uniform bias field. An example of a system with hollow cylinder template elements is shown in **Fig. 1**. The template elements can be geometrically tailored to produce localized regions of attractive and repulsive magnetic force. The ability to customize the force field in this way is a key feature of the assembly method as it enables

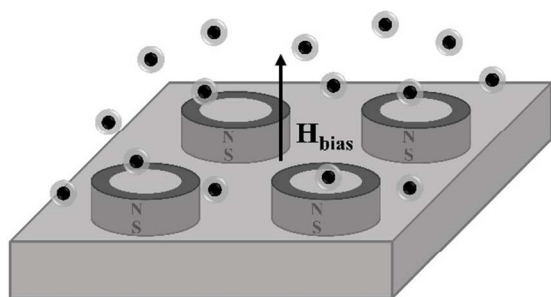


Figure 1. A self-assembly system showing soft-magnetic hollow cylinder template elements embedded in a nonmagnetic substrate.

extraordinary control of particle motion during assembly, which results in nanoscale precision in particle placement. We demonstrate the method using a computational model that takes into account dominant mechanisms of particle transport and can be used to simulate the assembly process. To date, various computational techniques have been successfully applied for the study of magnetic particle systems. These include Brownian dynamics^{27,28,29}, the discrete element method³⁰, the lattice-Boltzmann method³¹, Monte Carlo^{32,33} and molecular dynamic simulations³⁴, stochastic dynamics³⁵ and various analytical methods^{36,37,38}. The model used here is based on Langevin's equation and takes into account magnetic and hydrodynamic forces including inter-particle interactions, Brownian diffusion, Van der Waals force and the effects of surfactants. A dynamic time-stepping scheme is used to integrate the equations of motion, which greatly accelerates and stabilizes the simulations. We demonstrate the assembly process for the system shown in **Fig. 1** using core-shell $\text{Fe}_3\text{O}_4\text{-SiO}_2$ particles. The hollow cylinder template elements produce a force field that focuses the particles into a ring-like pattern. An analytical force expression is used to optimize the dimensions of the elements for this purpose. Once the template element dimensions are known, the computational model is used to simulate the assembly process as a function of the particle volume fraction. The analysis demonstrates that extended monolayer single particle chain-like patterns can be assembled within milliseconds with nanoscale precision by tailoring key parameters including the template geometry to produce a force field that provides precise positioning of the particles; the thickness of the dielectric shell to control the strength of the interparticle dipole-dipole force upon contact and the particle volume fraction to suppress undesired aggregation during assembly. To date, various experimental studies have demonstrated self-assembly of nanoparticles with nanoscale^{39,40,41} and microscale^{42,43,44} resolution using uniform and/or gradient fields as well as the field induced self-assembly of magnetic core-shell particles⁴⁵. Of particular relevance is experimental work by Henderson et al.³⁹, wherein a nanoparticle assembly was tailored using a combination of a spatially alternating gradient field, which was provided by a nanoscale patterned template in the form of magnetic recording media, with a uniform external field. This combination of fields closely matches the approach that we propose, albeit our gradient field is provided by lithographically-patterned standalone soft-magnetic elements and the particles are multi-layered, which provide advantages. Nevertheless this prior work can serve as particle proof-of-concept of our proposed assembly method. We demonstrate the method for three different template geometries (hollow cylinders, hollow cubes and cross-structures) and two different core-shell particle sizes.

The proposed method broadly applies to arbitrary template geometries and multi-layered core-shell particles that have at least one magnetic component. As such, it can enable the self-assembly of complex patterns of nanoparticles and opens up opportunities for the scalable fabrication of multifunctional nanostructured materials for a broad range of applications in fields that include photonics, magnetics, electronics, chemical and biological sensing, energy storage and harvesting and catalysis. The computational model enables the rational design of novel media for such applications.

2 The Computational Model

The behaviour of colloidal magnetic particles in the presence of an external field is complex function of a number of competitive factors including hydrodynamic and magnetic forces, Brownian motion, Van der Waals force and the effects of surfactants. We predict the self-assembly of such particles using a computational model based on Langevin's equation that takes these effects into account,

$$m_i \frac{d^2 \mathbf{x}_i}{dt^2} = \mathbf{F}_{mag,i} + \mathbf{F}_{vis,i} + \mathbf{F}_{B,i}(t) + \sum_{j=1}^N (\mathbf{F}_{dd,ij} + \mathbf{F}_{vdw,ij} + \mathbf{F}_{surf,ij} + \mathbf{F}_{hyd,ij}), \quad (1)$$

where m_i and $\mathbf{x}_i(t)$ are the mass and position of the i 'th particle. The right-hand-side of this equation represents the sum of forces on the i 'th particle: $\mathbf{F}_{mag,i}$ due to the applied magnetic field, which is a superposition of the bias field and induced gradient-fields; $\mathbf{F}_{vis,i}$, viscous drag due to relative motion between the particles and the surrounding fluid (Stokes drag); $\mathbf{F}_{B,i}(t)$ a stochastic force to account for Brownian motion; $\mathbf{F}_{dd,ij}$ the interparticle magnetic dipole-dipole force due to induced dipole moments; $\mathbf{F}_{vdw,ij}$ Van der Waals force; $\mathbf{F}_{surf,ij}$ a repulsive force due to surfactant contact between particles and $\mathbf{F}_{hyd,ij}$ due to interparticle hydrodynamic interactions. We predict the particle dynamics by numerically integrating Eq. (1) using an adaptive time stepping method to accelerate and stabilize the computation. The various terms in the model and its implementation are described in the following sections.

2.1 Magnetic force

The magnetic force on a particle due to an external field is computed using an "effective" dipole moment method in which the particle is modeled as an "equivalent" point dipole with an effective moment \mathbf{m}_{eff} . The force on the i 'th particle is given by³⁶

$$\mathbf{F}_{mag,i} = \mu_f (\mathbf{m}_{i,eff} \cdot \nabla) \mathbf{H}_a, \quad (2)$$

where μ_f is the permeability of the fluid and \mathbf{H}_a is the applied magnetic field intensity at the center of particle. The moment is given by $\mathbf{m}_{eff} = V_p M_p$ where $V_p = \frac{4}{3} \pi R_p^3$ and M_p are the volume and magnetization of the particle, respectively. In the case of magnetic-dielectric core-shell particles, $\mathbf{m}_{eff} = V_{core} M_p$, where $V_{core} = \frac{4}{3} \pi R_{core}^3$. The moment can be determined using a magnetization model that takes into account self-demagnetization and magnetic saturation of the particles^{36,37}

$$\mathbf{m}_{i,eff} = V_p f(H_a) \mathbf{H}_a, \quad (3)$$

where⁴⁶

$$f(H_a) = \begin{cases} \frac{3(\chi_p - \chi_f)}{(\chi_p + 2\chi_f) + 3} H_a < \left(\frac{\chi_p + 2\chi_f}{3(\chi_p - \chi_f)} + 3 \right) M_{sp} \\ M_{sp} / H_a & H_a \geq \left(\frac{\chi_p + 2\chi_f}{3(\chi_p - \chi_f)} + 3 \right) M_{sp} \end{cases}. \quad (4)$$

In this expression, χ_f is the susceptibility of the fluid and χ_p is the intrinsic magnetic susceptibility of the particle, i.e. $M_p = \chi_f H_{in}$, where H_{in} is the field inside the particle. H_{in} differs from H_a by the demagnetization field i.e. $H_{in} = H_a - N_d M_p$ where N_d is the demagnetization factor of the particle, i.e. $N_d = 1/3$ for a spherical particle. The value of χ_p can be obtained from a measured M vs. H curve. However, M is often plotted as a function of H_a in which case $M_p = \chi_a H_a$, where χ_a is the apparent susceptibility. The two values of susceptibility are related as follows $\chi_p = \chi_a / (1 - N_d \chi_a)$, which reduces to $\chi_p = 3\chi_a / (3 - \chi_a)$ for a spherical particle⁴⁷. The magnetic force can be rewritten as

$$\mathbf{F}_{mag} = \mu_f V_p f(H_a) (\mathbf{H}_a \cdot \nabla) \mathbf{H}_a, \quad (5)$$

This can be determined once an expression for \mathbf{H}_a is known. For the system shown in **Fig. 1**, the applied field is a superposition of the uniform bias field and the induced localized gradient-fields produced by the magnetized soft-magnetic template elements, i.e. $\mathbf{H}_a = \mathbf{H}_{bias} + \mathbf{H}_{template}$. We use analytical closed-form expressions to predict the fields and force as described in the Appendix. The use of analytical analysis reduces the complexity and increases the accuracy of the computation as compared to more commonly used numerical field analysis. In the latter, the magnetostatic field equations are discretized and solved using a computational mesh. Since the magnetic field has a long range, an extended computational domain is often used to account for this. Moreover, the field gradient, which defines the force, tends to be sensitive to the size of mesh. Mesh size sensitivity studies are usually required to ensure accurate force analysis and while a smaller mesh can provide increased accuracy, it also increases computational cost. An analytical analysis eliminates the need for this complexity. However, it should be noted that the use of analytical methods for the magnetic analysis is based on the assumption that the bias and template fields are unaffected by other materials, i.e. the substrate and carrier fluid are assumed to be nonmagnetic.

2.2 Magnetic dipole-dipole interaction

In the presence of an applied field, the magnetic core of the nanoparticles becomes magnetized and acquires an effective moment \mathbf{m}_{eff} as described above. The potential energy for two dipoles is given by

$$U_{dd,ij} = -\frac{\mu_f}{4\pi} \left(3 \frac{(\mathbf{m}_{i,eff} \cdot \mathbf{r}_{ij})(\mathbf{m}_{j,eff} \cdot \mathbf{r}_{ij})}{r_{ij}^5} - \frac{\mathbf{m}_{i,eff} \cdot \mathbf{m}_{j,eff}}{r_{ij}^3} \right), \quad (6)$$

where $\mathbf{m}_{i,eff}$ and $\mathbf{m}_{j,eff}$ are the moments of i 'th and j 'th particle, respectively, and \mathbf{r}_{ij} is the displacement vector between them. The dipole-dipole force in Eq. (1) is obtained as the gradient of the potential,

$$\mathbf{F}_{dd,ij} = -\nabla U_{dd,ij}. \quad (7)$$

2.3 Van der Waals interaction

Van der Waals force is taken into account as an attractive force, which is calculated using⁴⁸,

$$\mathbf{F}_{vdw,ij} = \frac{A}{6} \frac{d_i^6}{(h_{ij}^2 + 2d_i h_{ij})^2 (h_{ij} + d_i)^3}, \quad (8)$$

where A is the Hamaker constant and h_{ij} is the surface-to-surface separation distance between the i 'th and j 'th particle.

2.4 Surfactant force

The repulsive force caused by the surfactant-surfactant contact is taken into consideration in our model. The potential energy U_s of this interaction is given by⁴⁹,

$$U_s = 2\pi R_p^2 N_s k_B T \left\{ 2 - \frac{r_{ij} - 2R_p}{\delta} - \frac{r_{ij}}{\delta} \ln \left(\frac{2R_p + 2\delta}{r_{ij}} \right) \right\}, \quad (9)$$

where R_p , δ and N_s are, respectively, the radius of particle, the thickness of the surfactant layer and the surface density of surfactant molecules. The repulsive force is calculated as the gradient of this potential energy:

$$\mathbf{F}_{rep,ij} = -\nabla U_s = \frac{2\pi R_p^2 N_s k_B T}{\delta} \ln \left(\frac{2R_p + 2\delta}{r_{ij}} \right). \quad (10)$$

2.5 Viscous drag

The drag force on a particle due to the viscosity of the fluid is computed using Stokes' formula

$$\mathbf{F}_{D,i} = D \frac{d\mathbf{x}_i}{dt}, \quad (11)$$

Where $D = 6\pi\eta R_{hyd,p}$ is the drag coefficient, η is the fluid viscosity and $R_{hyd,p}$ is the hydrodynamic radius of the particle.

2.6 Interparticle Hydrodynamics Interactions

Hydrodynamic interactions between particles become important at small surface-to-surface separation distances. The force between two neighboring particles is based on lubrication theory and can be expressed as follows⁴⁸,

$$\mathbf{F}_{lub,ij} = \frac{6\pi\mu_f V_{r,i,j} d_i^2}{h_{ij} 16}, \quad (12)$$

where h_{ij} is the separation between the surfaces and $V_{r,i,j}$ is the relative velocity between the particles. When the particles are in contact ($h_{ij} \leq 0$) this force is considered to be negligible.

2.7 Brownian diffusion

Brownian motion needs to be considered when predicting the dynamics of nanoscale particles. We use the following equation to account for these effects in each dimension:

$$\langle x^2 \rangle = \frac{2k_B T \Delta t}{D} \quad \Delta \bar{\mathbf{x}}_{B,i} = \bar{\mathbf{n}} \cdot \delta \cdot \sqrt{\langle x^2 \rangle} = \bar{\mathbf{n}} \cdot \delta \cdot \sqrt{\frac{2k_B T \Delta t}{D}}, \quad (13)$$

where k_B is Boltzmann's constant, D is the Stokes' drag coefficient as described above, $\Delta \bar{\mathbf{x}}_{B,i}$ is implemented in Eq. (16), $\bar{\mathbf{n}}$ and δ is a randomly generated directional unit vector and a random distribution number between zero and one, which represents the direction and magnitude of the displacement due to Brownian motion. These displacements will be applied into the 3 Cartesian directions individually.

2.6 Equations of Motion

Particle motion during assembly is predicted by solving Langevin's equation, which can be rewritten as

$$m_i \frac{d^2 \mathbf{x}_i}{dt^2} + D \frac{d\mathbf{x}_i}{dt} = \mathbf{F}_{sum,i} + \mathbf{F}_{B,i}(t), \quad (14)$$

where

$$\mathbf{F}_{sum,i} = \mathbf{F}_{mag,i} + \sum_{j=1}^N (\mathbf{F}_{dd,ij} + \mathbf{F}_{vdw,ij} + \mathbf{F}_{rep,ij} + \mathbf{F}_{lub,ij}), \quad (15)$$

Eq.(14) can be solved by first reducing it to a pair of coupled first-order equations and then integrating these equations using a numerical time stepping scheme. The discretized first-order equations are as follows:

$$\Delta \mathbf{x}_i = \frac{\mathbf{F}_{sum,i}}{D} \tau + \frac{m_i}{D} \left(\mathbf{v}_{i,0} - \frac{\mathbf{F}_{sum,i}}{D} \right) \left(1 - e^{-\frac{D}{m_i} \tau} \right) + \Delta \mathbf{x}_{B,i}, \quad (16)$$

and

$$\mathbf{v}_{i,f} = \frac{\mathbf{F}_{sum,i}}{D} + \left(\mathbf{v}_{i,0} - \frac{\mathbf{F}_{sum,i}}{D} \right) e^{-\frac{D}{m_i} \tau}, \quad (17)$$

where τ is the integration time step, $\mathbf{v}_{i,0}$ and $\mathbf{v}_{i,f}$ are the velocity of the i 'th particle at the beginning and end of the time step and $\Delta \mathbf{x}_{B,i}$ is the displacement due to Brownian motion. In our analysis, the time step τ is dynamically adjusted based on the relative velocities and surface-to-surface separations h_{ij} of the particles. When the time step τ is large enough ($\tau \gg \frac{m_i}{D}$), Eq. (17) can be simplified to

$$\mathbf{v}_{i,f} = \frac{\mathbf{F}_{sum,i}}{D}. \quad (18)$$

3 Analysis of Self-assembly

We demonstrate the proposed assembly method for the system shown in **Fig. 1**. Here, the templates are hollow soft-magnetic cylinders that are embedded in a non-magnetic substrate. A uniform bias field \mathbf{H}_{bias} is applied upward, perpendicular to the substrate, to magnetize the elements along their axis. When a colloid of core-shell nanoparticles are introduced onto the substrate they assemble into structures, the geometry of which depends on parameters that include the strength of the bias field, the dimensions of the template elements, the core and shell dimensions and the volume fraction of the nanoparticles. The computational model can be used to predict the assembled structure given these parameters, or alternatively, to determine a specific mix of parameters that produce a pre-defined assembled structure. In this section, we demonstrate the latter and determine parameters that produce a prescribed monolayer ring-like particle pattern. For the purpose of analysis, and without loss of generality, the core shell particles are taken to be 60 nm Fe_3O_4 - SiO_2 with a core diameter of 30 nm ($R_{core} = 15$ nm) and a shell thickness of 15 nm. In principle, any multi-layered core-shell particle can be used as long as it has at least one magnetic component. Fe_3O_4 has a density $\rho_{core} = 5000$ kg/m³ and a saturation magnetization $M_{sp} = 4.78 \times 10^5$ A/m. The SiO_2 shell has a density $\rho_{shell} = 2648$ kg/m³. The template elements are chosen to be permalloy (78% Ni, 22% Fe), which has a saturation magnetization $M_{e,s} = 8.6 \times 10^5$ A/m. The bias field is taken to be $H_{bias} = 3.9 \times 10^5$ A/m ($B_{bias} = 5000$ Gauss), which is sufficiently strong to saturate both the nanoparticles and the template elements as discussed below. This field can be obtained by positioning a rare-earth NdFeB magnet immediately beneath the substrate³⁷. The effective dipole moment of the saturated particles is $m_{eff} = V_{core} M_{sp}$. To simplify the analysis, we assume that the hydrodynamic radius of the particles is the same as their physical radius $R_{hyda,p} = 30$ nm. However, it should be noted that in general, the hydrodynamic radius is larger because of the presence of surfactants. Similarly, we assume that the colloid is monodispersed, whereas in reality there will be a particle size distribution. The carrier fluid is assumed to be nonmagnetic ($\chi_f = 0$), with a viscosity and density equal to that of water, $\eta = 0.001$ N · s/m² and $\rho_f = 1000$ kg/m³.

3.1 Magnet Force Analysis

We first analyze the magnetic force. The goal is to determine template dimensions that produce a force field that focuses the particles into a prescribed pattern, in this case a ring-like structure. To demonstrate the analysis, we choose the inner and outer radial dimensions of the ring assembly to be $R_{ring,in} = 400$ nm and $R_{ring,out} = 500$ nm, respectively. Let R_{in} and R_{out} denote the inner and outer radii of the template element and let h denote its height. To obtain the desired assembly, set $R_{in} = R_{ring,in} = 400$ nm and

$R_{out} = R_{ring,out} = 500$ nm. These are chosen so that the particles assemble over the annulus of the element. The spacing of the elements is taken to be 2 μm center-to-center so that there is negligible overlap of their fields, which we verify below. Thus, it suffices to perform the

template design for a single isolated element. Analytical closed-form expressions for the field and force of a single hollow cylinder soft-magnetic element in a uniform bias field are presented in the Appendix. These are used to optimize the force field as a function of the element dimensions. These formulas can be easily adapted for the more

general case of closely spaced elements as described in the Appendix. We determine a template height h that provides a viable force field for assembly. For the force analysis, a reference frame is chosen with the x-y plane coincident with the surface of the substrate and with the z axis aligned with the axis of the element. Thus, the top surfaces of both the substrate and the template element are at $z = 0$. We use Eqs. (A3) and (A4) in the Appendix to compute the radial and axial force components $F_{mag,r}$ and $F_{mag,z}$ across a horizontal line that spans a unit cell of the system and falls along the diameter of the element, i.e. $-1 \mu\text{m} \leq x \leq 1 \mu\text{m}$. The force components are computed at a distance $z = 100$ nm above the element for a range of element heights: $h = 100, 200$ and 300 nm. The force profiles for $F_{mag,z}$ are plotted in **Fig. 2** and show relatively little change for $h \geq 200$ nm. Thus, we choose the element height to be $h = 200$ nm. Note that the force profiles are axisymmetric because of the cylindrical symmetry of the template geometry. The 3D force and corresponding field profiles are shown in **Fig. 3**. Also, recall that

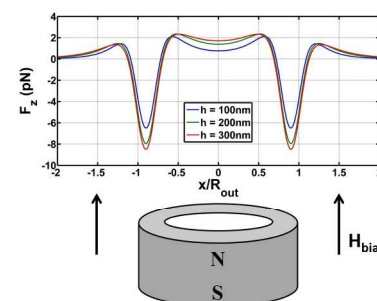


Figure 2. Axial magnetic force $F_{mag,z}$ along a horizontal line 100 nm above the template element as a function of the height h . R_{out} is outer radius of the element.

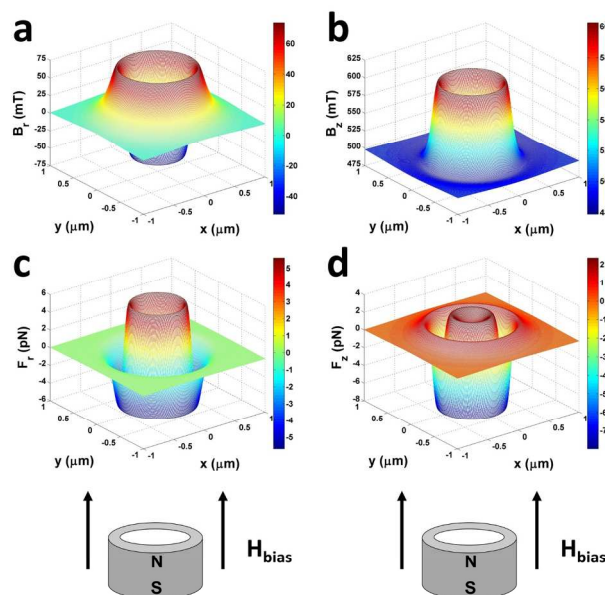


Figure 3. Axisymmetric magnetic field and force components at $z=100$ nm above the template element: (a) B_r , (b) B_z , (c) $F_{mag,r}$, and (d) $F_{mag,z}$.

this analysis is based on the assumption that the template element is saturated. It remains to verify this. From Eq. (A8) in the Appendix, this occurs when $H_{bias} \geq N_d M_{es}$, where N_d is the demagnetization factor of the element. For the chosen element dimensions ($R_{in} = 400 \text{ nm}$, $R_{out} = 500 \text{ nm}$, $h = 200 \text{ nm}$), $N_d < 0.4^{50}$ and it follows that the element is saturated because $H_{bias} \geq 0.4 M_{es}$.

Next, the magnetic force provided by a template element with dimensions: $R_{in} = 400 \text{ nm}$, $R_{out} = 500 \text{ nm}$, $h = 200 \text{ nm}$ is analyzed in more detail. The x and z components of the force $F_{mag,x}$ and $F_{mag,z}$ are computed along the same horizontal line as above, i.e. $-1 \mu\text{m} \leq x \leq 1 \mu\text{m}$, for a range of distances above the element, $z = 100, 150$ and 300 nm . The force profiles are plotted in Fig. 4 and the analysis shows that there is a relatively strong (downward-directed) axial force $F_{mag,z}$ over the annulus of the element, $R_{in} \leq r \leq R_{out}$ as indicated by the red arrows, which promotes assembly in this region. Significantly, there is also a relatively weak repulsive (upward-directed) axial force above a substantial portion of its interior region ($0 \leq r \leq R_{in}$) as indicated by the blue arrows, which prevents particles from assembling there. The repulsive force is due to the superposition of the uniform bias field and the gradient-field of the element. Specifically, the bias field induces an upward-directed moment $m_{eff}\vec{z}$, whereas the magnetized element produces a spatially varying field gradient ∇H_d that changes in sign depending on the location relative to the element. Since the force is proportional to the product of these two terms as shown in Eq. (2), it is attractive (negative) in regions where these terms have opposite signs and repulsive (positive) when they have the same sign. The radial field component $F_{mag,r}$ also plays a critical role in focusing the particles over the annulus. Note from Fig. 3a that it is directed outward over the interior of the annulus $0 \leq r \leq R_{in}$, and inward over the exterior of the annulus $r \geq R_{out}$. This is also reflected in the plot of $F_{mag,x}$, which is directed outward over the interior of the annulus $0 \leq x \leq R_{in}$, and inward over the exterior of the annulus $x \geq R_{out}$. as indicated by the arrows Thus, the magnetic force field directs the particles over the annulus, which promotes assembly of the ring structure. It is important to note that the ability to produce regions of attractive and repulsive magnetic force is a key feature of the proposed assembly method as it enables nanoscale precision of particle placement.

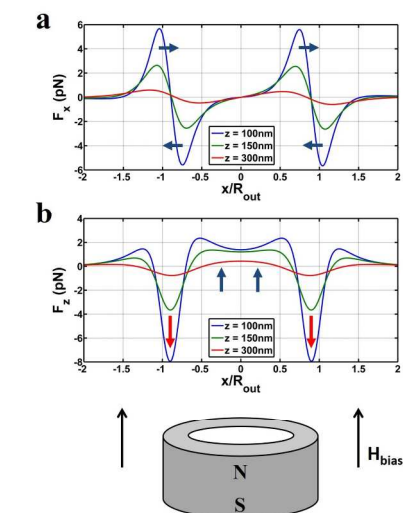


Figure 4. Magnetic force along horizontal lines 100, 150 and 300 nm above the template (arrows indicate direction of force): (a) $F_{mag,x}$ and (b) $F_{mag,z}$

It is instructive to investigate the impact of neighboring template elements on the magnetic force. It is assumed that there is negligible overlap of the magnetic force. It remains to verify this. To this end, we compute the axial force field $F_{mag,z}(x, y, z)$ for a 3 by 3 array of elements ($2 \mu\text{m}$ center-to-center spacing) at a distance $z = 100 \text{ nm}$ above the elements. The force, which is shown in Fig. 5, is computed by first forming the total field via superposition of the individual element fields and then computing the force using the

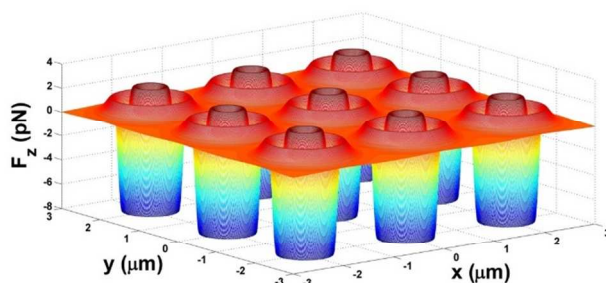


Figure 5. Magnetic force field $F_{mag,z}(x, y, z)$ at $z = 100 \text{ nm}$ above a 3 by 3 array of template elements.

total field as described in the Appendix. The analysis shows that the force falls off dramatically between the elements and that there is negligible overlap of their effects.

Lastly, we estimate the effective range of the magnetic force, i.e. the distance z beyond which directed assembly is thwarted by Brownian motion. The particles within this distance contribute to a rapid assembly (on the order of milliseconds), while those beyond this range have a negligible contribution. We use the following criterion to estimate this distance,

$$|F_{mag,z}(z)|D_p \sim k_B T, \quad (19)$$

Here, $|F_{mag,z}(z)|$ is the magnitude of the magnetic force acting on a particle of diameter D_p at a distance z above the element and k_B and T are as defined in Eq. (13). This relation is basically a comparison between thermal energy and the energy expended by the magnetic force in moving a particle a distance D_p . The particles within a distance z from the element such that $|F_{mag,z}(z)|D_p > k_B T$ will predominantly contribute to the assembly, much less so for those beyond this height will not. We evaluate $F_{mag,z}(z)$ over the center of the annulus $R_{ave} = (R_{in} + R_{out})/2$ where the attractive force is maximum. A plot of the ratio $F_{mag,z}(R_{ave}, z)D_p/k_B T$ vs. z is shown in Fig. 6. From this plot we see that the magnetic force is dominant below $0.75 \mu\text{m}$ and the Brownian force is dominant above this height. Thus, we estimate that the effective range of directed assembly for this template is approximately $z \leq 1 \mu\text{m}$. We study the dynamics of assembly next.

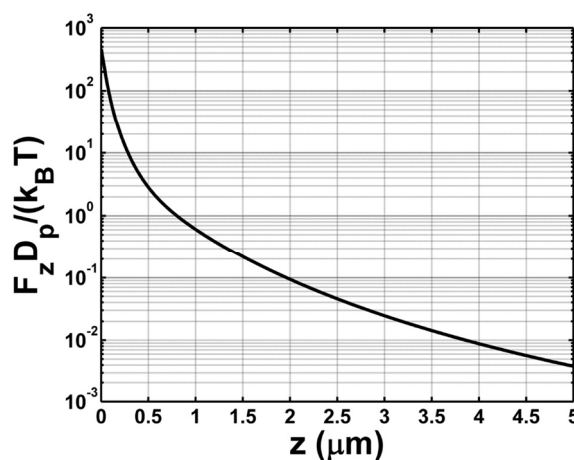


Figure 6. Ratio of magnetic to thermal energy along a vertical line over the annulus of a template element.

3.2 Dynamics of the Assembly Process

In this section we use the computational model to study the dynamics of the assembly process. The bias field and template dimensions are as above. We use a computational domain centered with respect to a single element. The domain spans a unit cell, i.e. 2 μm along both the x and y axes and 1 μm in the z -direction as shown in **Fig. 7a and 8a**. The base of the domain is at $z = 0$, which coincides with the top surface of both the substrate and the template element. Periodic boundary conditions for particle transport are imposed at the lateral sides of the domain to account for a 2D array of template elements. We simulate the assembly of 60 nm Fe_3O_4 - SiO_2 particles for a range of different percent volume fractions: $\phi = 0.0655, 0.0873, 0.11, 0.131, 0.153$ and 0.175% . These values correlate to an integer number of particles in the computational domain, e.g. $\phi = 0.0655$ and 0.175% correspond to 15 and 40 particles, respectively. The modeling shows that the final assembly for all of the ϕ values is chain-like ring pattern. Representative plots of the initial and final particle distributions for $\phi = 0.0873$ and 0.1750% are shown in **Figs. 7 and 8**, respectively. Animations of the particle dynamics during assembly are provided in the supporting

information.

In this analysis the particles are initially randomly distributed and their final configuration is a single particle ring pattern that forms over the annulus of the template element. The assembly was completed in less than 30 ms for all the cases studied. The final particle assembly has many important features. For example, it has a line width of 60 nm, i.e. the diameter of the nanoparticles. This is smaller than the line width of the template element, i.e. the width of the annulus which is 100 nm. Another interesting feature is that the particles are nearly uniformly spaced. This occurs because neighbouring particles are pushed apart by a mutually repulsive dipole-dipole force, which is due to the alignment of all dipole moments upward, parallel to the applied field. The spacing between the particles S_p in the first layer (i.e. monolayer) varies somewhat because of the effects of Brownian motion. However, as the particle volume fraction increases, both this spacing and the variation in spacing decrease as shown in **Fig. 9**. In this plot, the nearest neighbouring spacing is normalized with respect to the particle diameter D_p and the error bars reflect the range of spacing in the final assembly as computed by the model. The decrease in spacing and its variation is due to an increase in strength of the repulsive dipole-dipole force, which ultimately dominates the Brownian force and produces a denser particle packing. As the volume fraction

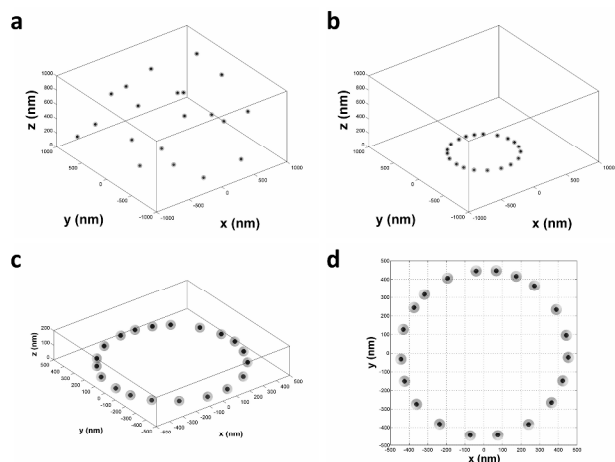


Figure 7. Initial and final particle distributions for $\phi = 0.0873\%$: (a) initial random particle distribution, (b) perspective of final assembled particle ring, (c) lateral view of assembled particle ring, (d) magnified top view of assembled ring.

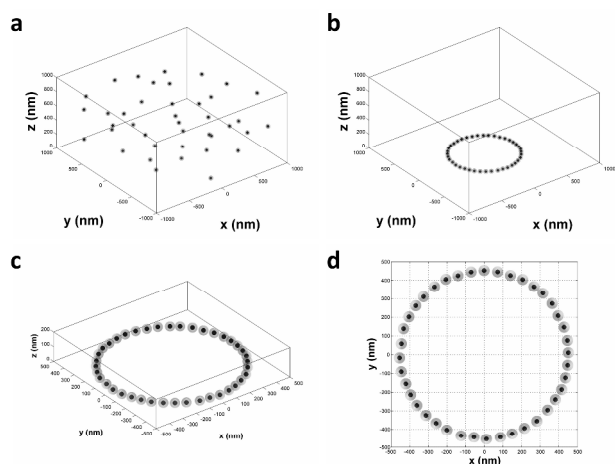


Figure 8. Initial and final particle distributions for $\phi = 0.1750\%$: (a) initial random particle distribution, (b) perspective of final assembled particle ring, (c) lateral view of assembled particle ring, (d) magnified top view of assembled ring.

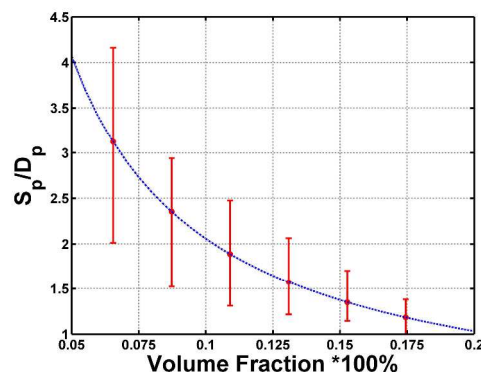


Figure 9. Normalized particle spacing S_p and variation in spacing vs. volume fraction.

increases further, the particles will eventually begin to form an additional layer of the ring. It is useful to determine a first-order estimate of the volume fraction at which this occurs. To this end, we study the energetics of competing assembly configurations. Let N be the number of particles in the assembly. In the first configuration, all N particles are arranged in a ring pattern with uniform spacing between them. In the second configuration, $N-1$ particles are in a ring pattern and the remaining particle is vertically stacked on one of these particles, thereby forming a vertical two particle chain. The second configuration represents the transition from a single layer of particles to the beginning of a second layer. We compare the magnetostatic energy of the two configurations, E_r and E_c , respectively. The magnetostatic energy of each assembly is computed using $E_{mag} = \sum_{i=1}^N \sum_{j=i+1}^N U_{dd,ij} + \sum_{i=1}^N m_i \cdot B_{a,i}$, where $U_{dd,ij}$ is the potential energy due to dipole-dipole interaction between the i 'th and j 'th particles as given in Eq. (6) and $m_i \cdot B_{a,i}$ is the energy of the i 'th dipole due to its interaction with the applied field $B_{a,i}$, which is evaluated at the center of the particle. It is instructive to compare the relative energy difference $\Delta E = E_c - E_r$ between the two configurations at different heights above the elements as a function of the number of particles, which translates into a volume fraction. When $\Delta E > 0$, the energetics favor a single layer ring-like pattern because E_c is higher than E_r . However, when

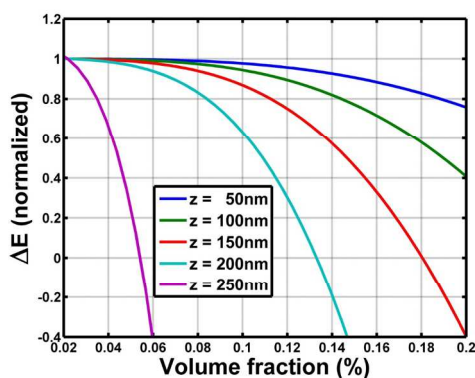


Figure 10. Normalized relative energy ΔE as a function of volume fraction and distance z above the template element.

$\Delta E < 0$ the two particle chain configuration is favored, which corresponds to the initial formation of an additional layer of particles. Parametric plots of normalized ΔE are shown in **Fig. 10**. This figure can be used to obtain a first-order estimate of the onset of a subsequent layer of particles (assembled upon the current layer) as a function of an initial volume fraction of the particles and the height of the current layer above the substrate. From this data we find that at $z = 50$ and 100 nm $\Delta E > 0$ for all volume fractions up to 0.2%. Thus, a monolayer ring pattern is favoured at these heights, which is consistent with the simulations above. Partial vertical stacking occurs at $z = 150, 200$ and 250 nm at volume fractions above 0.18%, 0.13% and 0.055%, respectively, which implies that an additional layer will form under these conditions. It is important to emphasize that the analysis above is simply a first order estimate of the impact of the volume fraction on the formation of an additional particle layer. It is based on magnetostatic analysis alone, i.e. ignoring Van der Waals force and the effects of surfactants. It does not account for the possibilities that the particles assemble into multiple rings or zip-chain patterns etc. A full simulation needs to be performed to obtain a rigorous understanding of the formation of multilayered systems.

Finally, in the analysis above we have demonstrated the assembly process for a hollow cylinder template element. However, the approach broadly applies to arbitrary template geometries. To confirm this, we now model self-assembly for two other template geometries, a hollow cube and a cross structure. Both geometries are 200 nm deep and have a 100 nm wall thickness. The cube is 1000 nm on a side and each segment of the cross is also 1000 nm long. The particles are as above i.e. 60 nm $\text{Fe}_3\text{O}_4\text{-SiO}_2$, as is the computational domain, which spans $2 \mu\text{m}$ along both the x and y axes and $1 \mu\text{m}$ in the z -direction. The initial and final particle distributions for these geometries are shown in **Figs. 11 and 12**, respectively. The particle volume fractions for these simulations are 0.2185% and 0.1750%, respectively. We used semi-numerical models to compute the 3D field distribution and force of the template elements as described by Furlani⁵¹. A similar analysis is performed with smaller particles, i.e. with a 30 nm core and 10 nm thick shell. The assembly of these particles for the same cross structure as above is shown in **Fig. 13** assuming a volume fraction of 0.0650%. The particles form a zip-chain like patterns at the ends of the cross and a multilayer structure at its centre due to the smaller size of the particles.

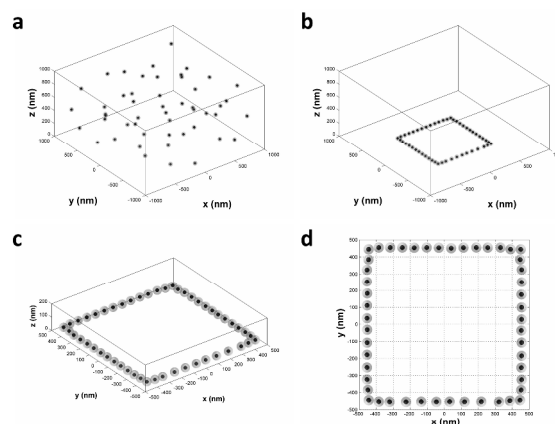


Figure 11. Initial and final particle distributions for a hollow cube template element for a volume fraction of $\phi = 0.2185\%$: (a) initial random particle distribution, (b) perspective of final assembled particle pattern, (c) lateral view of assembled particle pattern, (d) magnified top view of assembled rectangular pattern.

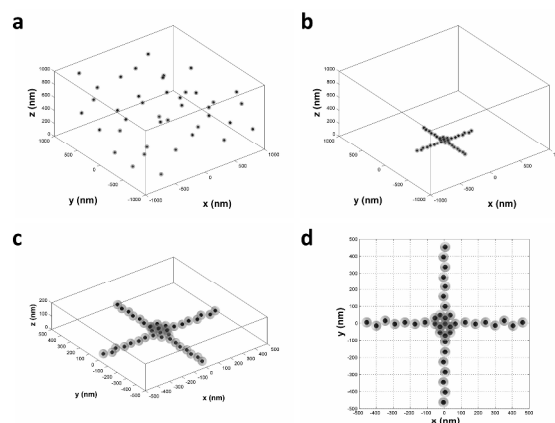


Figure 12. Initial and final particle distributions for a cross template element for a volume fraction of $\phi = 0.1750\%$: (a) initial random particle distribution, (b) perspective of final assembled particle pattern, (c) lateral view of assembled particle pattern, (d) magnified top view of assembled cross pattern.

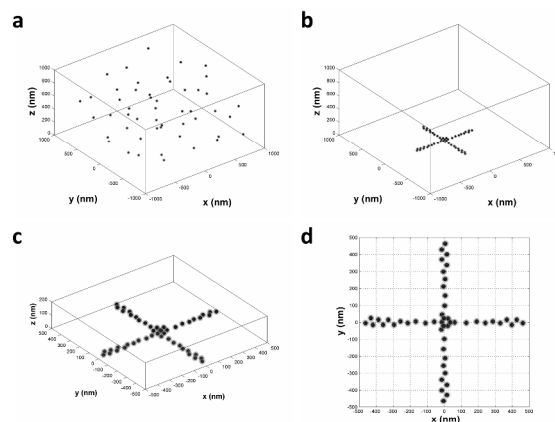


Figure 13. Initial and final particle distributions for a cross template element for a volume fraction of $\phi = 0.0650\%$: (a) initial random particle distribution, (b) perspective of final assembled particle pattern, (c) lateral view of assembled particle pattern, (d) magnified top view of assembled cross pattern.

4 Discussion

The analysis above demonstrates the viability of controlling the assembly of the core-shell nanoparticles into extended monolayer geometric patterns with nanoscale precision. To achieve this, various parameters need to be carefully chosen and computational modeling is invaluable for determining these. There are three groups of parameters that are especially important: the particle properties, the template properties and the particle volume fraction. With regards to the particles, both the core properties, magnetization M_p and especially radius R_{core} and the shell thickness are important. The first two parameters directly impact the magnetic and dipole-dipole forces, i.e. $F_{mag} \sim M_p R_{core}^3$ and $F_{dd} \sim M_p^2 R_{core}^6$. These parameters can be tuned to control the particle motion and interparticle coupling during assembly. The shell thickness also impacts the dipole-dipole force, but only when the particles are in contact. It can be increased to reduce F_{dd} in order to suppress undesired chaining and promote the formation of a monolayer. The overall particle size also impacts the hydrodynamic forces, e.g. larger particles exhibit greater viscous drag and assemble more slowly. As for the template elements, the most important properties are the dimensions and to a lesser extent the level of magnetization M_e . The template dimensions are especially critical as they can be tailored to produce localized regions of attractive and repulsive force that enable nanoscale precision in particle placement. On the other hand, M_e depends on the template material and the strength of the bias field and has a nonlinear contribution to the magnetic force $F_{mag} \sim M_e^2$. Finally, the particle volume fraction can be adjusted to control undesired aggregation during the assembly process. Specifically, as the volume fraction increases the particles are closer together and tend to aggregate during assembly, which interferes with the formation of the desired monolayer pattern. Thus, the volume fraction must be kept low enough to avoid this. All the aforementioned parameters can be determined for a given application using a combination of magnetic field modeling and particle transport modeling as demonstrated above.

5 Conclusions

We have presented a method for controlling the assembly of colloidal magnetic-dielectric core-shell nanoparticles into extended geometric patterns with nanoscale precision. This is achieved using soft-magnetic template elements with nanoscale line-widths to guide the assembly in the presence of a uniform bias field. The combination of a uniform field and localized high gradient fields produced by the template elements enables nanoscale precision of particle placement. We demonstrate proof-of-concept using a computational model that takes into account dominant mechanisms that govern the assembly dynamics. We show the first time that prescribed geometric patterns of particles can be assembled within milliseconds and with a line width resolution substantially greater than that of the template geometry. The increased resolution is due to the nanoscale precision in particle placement, which is achieved by tailoring key parameters including the template geometry to produce a force field that focuses the particles into prescribed patterns; the thickness of the dielectric particle shell to control the magnetic dipole-dipole force upon contact by providing a separation between the magnetic cores; and the particle volume fraction to suppress undesired aggregation during assembly. We have demonstrated the model using hollow cylinder, hollow cube and cross-shaped templates and dual-layer core-shell particles. However, it broadly applies to templates with an arbitrary geometry and multiple-layer particles that have at least

one magnetic component. Furthermore, once particle patterns have been formed, they can be transferred to a different substrate using techniques similar to those described by Henderson *et al.*³⁹ In this previous experimental study, field-directed patterning of magnetic nanoparticles was achieved using the magnetic field gradients at the surface of commercial disk drive media. The particle patterns were successfully transferred to the surface of a polymer film by spin-coating and peeling. The assembled particle patterns were preserved after peeling because the particles were immobilized during the spin-coating process by the large field gradients provided by the recording media. However, the lower limit gradient threshold required for viable pattern transfer is not known. It seems reasonable to assume that a similar pattern transfer process may apply to our approach, albeit this may require the fabrication of nanoscale template elements to provide sufficient particle immobilization, which could be challenging. In this case, a single template substrate could be used to reproduce numerous nano-patterned materials. In summary, we have used modelling to demonstrate the feasibility of new and interesting phenomena in the form of template-assisted assembly of single aligned magnetic core-shell particle structures at the millisecond time scale and the use of a nonmagnetic (e.g. silica) shells to further control interparticle forces. Prior experimental work³⁹ reinforces the viability of our approach. The ability to produce such nanostructured materials opens up opportunities for the scalable high-throughput fabrication of multifunctional nanostructured materials for a broad range of applications and our computational model enables the rational design of such media.

Acknowledgements

The authors acknowledge financial support from the U.S. National Science Foundation, through award number CBET-1337860.

Appendix

In this section we present analytical closed-form expressions for the magnetic field and force due to a soft-magnetic hollow cylindrical template element in a uniform bias field as shown in Fig.1. The total applied field \mathbf{H}_a is a superposition of the bias field \mathbf{H}_{bias} and the gradient-field \mathbf{H}_e due to the element. The bias field is directed upward along the z-axis and since the cylindrical element is axisymmetric we can express the total field as

$$\mathbf{H}_a = \mathbf{H}_{bias} + \mathbf{H}_e = H_{e,r} \hat{r} + (H_{bias,z} + H_{e,z}) \hat{z}. \quad (\text{A1})$$

The force on a magnetic particle is given by Eq. (5)

$$\mathbf{F}_{mag} = \mu_f V_p f(H_a) (\mathbf{H}_a \cdot \nabla) \mathbf{H}_a, \quad (\text{A2})$$

which can be decomposed into radial and axial components

$$\mathbf{F}_{mag,r} = \mu_f V_p f(H_a) \left(\mathbf{H}_{a,r} \cdot \frac{\partial \mathbf{H}_{a,r}}{\partial r} + \mathbf{H}_{a,z} \cdot \frac{\partial \mathbf{H}_{a,r}}{\partial z} \right), \quad (\text{A3})$$

and

$$\mathbf{F}_{mag,z} = \mu_f V_p f(H_a) \left(\mathbf{H}_{a,r} \cdot \frac{\partial \mathbf{H}_{a,z}}{\partial r} + \mathbf{H}_{a,z} \cdot \frac{\partial \mathbf{H}_{a,z}}{\partial z} \right). \quad (\text{A4})$$

The function $f(H_a)$ depends on the magnetization of the element \mathbf{M}_e which is induced by \mathbf{H}_{bias} as describe in Eq. (A1). We model the magnetization of the element using a linear model that takes into account saturation. Specifically, below saturation,

$$\mathbf{M}_e = \chi_e \mathbf{H}_{in}, \quad (\text{A5})$$

whereas above saturation $\mathbf{M}_e = \mathbf{M}_{es}$, where \mathbf{M}_{es} is the saturation magnetization and $\chi_e = \mu_e / \mu_0 - 1$ and μ_e are the susceptibility and permeability of the template element, respectively. In Eq.(A5), $\mathbf{H}_{in} = \mathbf{H}_{bias} + \mathbf{H}_{demag}$ is the field inside the element, $\mathbf{H}_{demag} = -N_d \mathbf{M}_e$ is the demagnetization field and N_d is the demagnetization factor of the element, which depends on its geometry⁵¹. Thus, below saturation

$$\mathbf{M}_e = \frac{\chi_e}{(1 + N_d \chi_e)} \mathbf{H}_{bias}, \quad (\text{A6})$$

which, for a soft-magnetic element ($\chi_e \gg 1$), reduces to

$$\mathbf{M}_e = \frac{\mathbf{H}_{bias}}{N_d} \quad (\chi_e \gg 1). \quad (\text{A7})$$

Thus, the magnetization of the element is obtained using,

$$\mathbf{M}_e = \begin{cases} \frac{\mathbf{H}_{bias}}{N_d} & \mathbf{H}_{bias} < N_d \mathbf{M}_{cs} \\ \mathbf{M}_{cs} & \mathbf{H}_{bias} \geq N_d \mathbf{M}_{cs} \end{cases}. \quad (\text{A8})$$

Once \mathbf{M}_e is known, \mathbf{H}_e can be computed. The field distribution \mathbf{H}_e of a hollow cylinder element that is magnetized upward along its axis (positive z direction) can be obtained via superposition using the field due to a solid cylinder $H_{cyl}(R_{cyl})$ of radius R_{cyl} . Let R_{in} and R_{out} denote the inner and outer radii of the hollow cylindrical element and let h denote its height. Then

$$\mathbf{H}_e = \mathbf{H}_{cyl}(R_{out}) - \mathbf{H}_{cyl}(R_{in}), \quad (\text{A9})$$

where $-\mathbf{H}_{cyl}(R_{in})$ represents the field due to a cylinder that is magnetized downward (negative z direction) and accounts for the missing core of the hollow cylinder. A semi-analytical expression for $\mathbf{H}_{cyl}(R_{cyl})$ has been derived using an equivalent current source model (see section 3.3 of Furlani (2001)⁵¹) as described by Furlani and Xue⁵². The solution method is summarized here for convenience. A cylinder with a uniform axial magnetization produces the same external field as that of a conventional surface current that flows around the circumference of the cylinder. We discretize the "equivalent" surface current into a finite set of current loop elements, and compute the total field by summing the field contribution from the individual elements, which is well-known (see p 263 in Stratton (1941)⁵³). The field distribution for a magnetized cylinder of

radius R_{cyl} and height h that is magnetized to saturation M_s and centered about the z-axis with its top surface at $z = 0$ can be written as

$$\begin{aligned} H_{cyl,r}(R_{cyl}, r, z) &= \frac{M_s}{2\pi} \int_{-h}^0 \Pi_r(r, z, z') dz' \\ H_{cyl,z}(R_{cyl}, r, z) &= \frac{M_s}{2\pi} \int_{-h}^0 \Pi_z(r, z, z') dz' \end{aligned}, \quad (\text{A10})$$

where the R_{cyl} functional dependence is implicit in the terms

$$\Pi_r(r, z, z') = \frac{(z - z')f(z, z')}{r} [R_c(z, z')E(k) - K(k)], \quad (\text{A11})$$

$$\Pi_z(r, z, z') = f(z, z') [Z_c(z, z')E(k) + K(k)]. \quad (\text{A12})$$

In these expressions $E(k)$ and $K(k)$ are the complete elliptic integrals of the first and second kind, respectively⁵⁴,

$$K(k) = \int_0^{\frac{\pi}{2}} \frac{1}{\sqrt{1 - k^2 \sin^2(\phi)}} d\phi, \quad E(k) = \int_0^{\frac{\pi}{2}} \sqrt{1 - k^2 \sin^2(\phi)} d\phi, \quad (\text{A13})$$

And

$$\begin{aligned} d &= (R_{cyl} - r)^2 + \delta(z, z')^2, \quad f(z, z') = \frac{1}{((R_{cyl} + r)^2 + \delta(z, z')^2)^{1/2}}, \\ k &= \left(\frac{4rR_{cyl}}{(R_{cyl} + r)^2 + \delta(z, z')^2} \right)^{1/2}, \quad R_c(z, z') = \frac{R_{cyl}^2 + r^2 + \delta(z, z')^2}{d}, \\ Z_c(z, z') &= \frac{R_{cyl}^2 - r^2 - \delta(z, z')^2}{d}, \quad \delta(z, z') = (z - z'). \end{aligned} \quad (\text{A14})$$

The field components in Eq. (A10) are evaluated using numerical integration. To compute the force, the gradient of the field is needed, which can be determined using the following relations,

$$\frac{\partial H_r(r, z, z')}{\partial r} = -\frac{1}{r} + (R_m + r)f^2 \Pi_r + \frac{(z - z')f}{r} \left[\frac{\partial R_c}{\partial r} E(k) + \frac{\partial k}{\partial r} (R_c dE(k) - dK(k)) \right], \quad (\text{A15})$$

$$\frac{\partial H_r(r, z, z')}{\partial z} = f^2 \frac{R_m + r}{z - z'} \Pi_r + \frac{(z - z')f}{r} \left[\frac{\partial R_c}{\partial z} E(k) + \frac{\partial k}{\partial z} (R_c dE(k) - dK(k)) \right], \quad (\text{A16})$$

$$\frac{\partial H_z(r, z, z')}{\partial r} = -f^2 (R_m + r) \Pi_z + f \left[\frac{\partial Z_c}{\partial r} E(k) + \frac{\partial k}{\partial r} (Z_c dE(k) + dK(k)) \right], \quad (\text{A17})$$

$$\frac{\partial H_z(r, z, z')}{\partial z} = -f^2 (z - z') \Pi_z + f \left[\frac{\partial Z_c}{\partial z} E(k) + \frac{\partial k}{\partial z} (Z_c dE(k) + dK(k)) \right]. \quad (\text{A18})$$

Eqs. (A15)-(A18) can be used to predict the field and force distribution due to a solid magnetic cylinder and this can be used in Eq. (A9) to determine the field of a hollow cylinder. Additional useful models of magnetic structures can be found in various references⁵⁵⁻⁵⁹.

The magnetic field and force due to an array of template elements can be obtained by superimposing their fields. Let N be the total number of elements in the array, and let $n = 0, 1, 2, 3, 4, \dots, N-1$ identify the individual elements. Choose a reference frame in which the central element, which is labelled $n=0$, is located at the origin in the x-y plane. The field components of this element are given by Eq. (A10). These need to be carefully converted to Cartesian coordinates to implement the superposition. The field solution for this element in Cartesian coordinates at an arbitrary observation point (x,y,z) is denoted by,

$$\mathbf{H}_e^{(0)}(x, y, z) = H_{e,x}^{(0)}(x, y, z) \hat{x} + H_{e,y}^{(0)}(x, y, z) \hat{y} + H_{e,z}^{(0)}(x, y, z) \hat{z}. \quad (\text{A19})$$

The n'th magnet in the array is centred at $x = x_n$ and $y = y_n$ in the x-y plane. The field components for this element can be written in terms of the field of the 0'th element as follows:

$$\mathbf{H}_e^{(n)}(x, y, z) = \mathbf{H}_e^{(0)}(x - x_n, y - y_n, z) \quad (n = 1, 2, 3, \dots, N-1). \quad (\text{A20})$$

The total field distribution of the array is obtained by summing the field contributions from all the elements,

$$\mathbf{H}_e(x, y, z) = \sum_{n=0}^{N-1} \mathbf{H}_e^{(n)}(x - x_n, y - y_n, z). \quad (\text{A21})$$

The total applied field is $\mathbf{H}_a = \mathbf{H}_{bias} + \mathbf{H}_e$. Finally, the total magnetic force on a particle due the array of elements is given by

$$\mathbf{F}_m = \mu_f V_p f(H_a) (\mathbf{H}_a \cdot \nabla) \mathbf{H}_a. \quad (\text{A22})$$

Note and references

^aDept. of Chemical and Biological Engineering, Univ. at Buffalo SUNY

^bDept. of Electrical Engineering, Univ. at Buffalo SUNY, NY 14260

- Pankhurst, Q.A.; Thanh, N.K.T.; Jones, S.K.; Dobson, J. Progress in applications of magnetic nanoparticles in biomedicine. In *J. Phys. D Appl. Phys.*, **2009**, 42(22), 224001/224001-224001/224015.
- Berry, C.C. Progress in functionalization of magnetic nanoparticles for applications in biomedicine. In *J. Phys. D Appl. Phys.*, **2009**, 42(22), 224003/224001-224003/224009.
- Pamme, N. Magnetism and microfluidics. In *Lab Chip*, **2006**, 6(1), 24-38.
- Furlani, E.P. Magnetic biotransport: analysis and applications. In *Materials*, **2010**, 3, 2412-2446.
- Arruebo, M; Fernández-Pacheco, R; Ibarra, M.R; Santamaría, J. Magnetic nanoparticles for drug delivery. In *Nanotoday*, **2007**, 2(3):22-32.
- Dobson, J. Magnetic micro- and nano-particle-based targeting for drug and gene delivery. In *Nanomedicine (London, U. K.)*, **2006**, 1(1), 31-37.
- Dobson, J. Gene therapy progress and prospects: magnetic nanoparticle-based gene delivery. In *Gene Ther.*, **2006**, 13(4), 283-287.
- Plank, C.; Zelphati, O.; Mykhaýlyk, O. Magnetically enhanced nucleic acid delivery. Ten years of magnetofection-Progress and prospects. In *Adv. Drug Delivery Rev.*, **2011**, 63(14-15), 1300-1331.
- Furlani, E.P.; Xue, X. Field, force and transport analysis for magnetic particle-based gene delivery. In *Microfluid. Nanofluid.*, **2012**, 13(4), 589-602.
- Ganguly, R.; Puri, I.K. Microfluidic transport in magnetic MEMS and bioMEMS. In *Wiley Interdiscip. Rev. Nanomed. Nanobiotechnol.*, **2010**, 2(4), 382-399.
- Zborowski, M; Chalmers J.J. Magnetic cell separation, vol 32 (Laboratory techniques in biochemistry and molecular biology). In *Elsevier Science*, **2007**, New York
- Xia, Y.; Gates, B.; Li, Z.-Y. Self-assembly approaches to three-dimensional photonic crystals. In *Adv. Mater. (Weinheim, Ger.)*, **2001**, 13(6), 409-413.
- Yethiraj, A.; Thijssen, J.H.J.; Wouterse, A.; Van Blaaderen, A. Large-area electric-field-induced colloidal single crystals for photonic applications. In *Adv. Mater. (Weinheim, Ger.)*, **2004**, 16(7), 596-600.
- Lu, Y.; Yin, Y.; Xia, Y. A self-assembly approach to the fabrication of patterned, two-dimensional arrays of microlenses of organic polymers. In *Adv. Mater. (Weinheim, Ger.)*, **2001**, 13(1), 34-37.
- Hochbaum, A.I.; Fan, R.; He, R.; Yang, P. Controlled growth of Si nanowire arrays for device integration. In *Nano Lett.*, **2005**, 5(3), 457-460.
- Shipway, A.N.; Katz, E.; Willner, I. Nanoparticle arrays on surfaces for electronic, optical, and sensor applications. In *ChemPhysChem*, **2000**, 1(1), 18-52.
- Aizenberg, J.; Braun, P.V.; Wiltzius, P. Patterned Colloidal Deposition Controlled by Electrostatic and Capillary Forces. In *Phys. Rev. Lett.*, **2000**, 84(13), 2997-3000.
- Hoogenboom, J.P.; Retif, C.; de Bres, E.; van de Boer, M.; Van Langen-Suurling, A.K.; Romijn, J.; van Blaaderen, A. Template-Induced Growth of Close-Packed and Non-Close-Packed Colloidal Crystals during Solvent Evaporation. In *Nano Lett.*, **2004**, 4(2), 205-208.
- Yellen, B.B.; Hovorka, O.; Friedman, G. Arranging matter by magnetic nanoparticle assemblers. In *Proc. Natl. Acad. Sci. U. S. A.*, **2005**, 102(25), 8860-8864.
- Jiang, P.; Prasad, T.; McFarland, M.J.; Colvin, V.L. Two-dimensional nonclose-packed colloidal crystals formed by spincoating. In *Appl. Phys. Lett.*, **2006**, 89(1), 011908/011901-011908/011903.
- Miszta, K.; de Graaf, J.; Bertoni, G.; Dorfs, D.; Brescia, R.; Marras, S.; Ceseracciu, L.; Cingolani, R.; van Roij, R.; Dijkstra, M.; Manna, L. Hierarchical self-assembly of suspended branched colloidal nanocrystals into superlattice structures. In *Nat. Mater.*, **2011**, 10(11), 872-876.
- Chen, Q.; Bae, S.C.; Granick, S. Directed self-assembly of a colloidal kagome lattice. In *Nature (London, U. K.)*, **2011**, 469(7330), 381-384.
- Demiroers, A.F.; Pillai, P.P.; Kowalczyk, B.; Grzybowski, B.A. Colloidal assembly directed by virtual magnetic moulds. In *Nature (London, U. K.)*, **2013**, 503(7474), 99-103.
- Erb, R.M.; Son, H.S.; Samanta, B.; Rotello, V.M.; Yellen, B.B. Magnetic assembly of colloidal superstructures with multipole symmetry. In *Nature (London, U. K.)*, **2009**, 457(7232), 999-1002.
- Dai, Q.; Frommer, J.; Berman, D.; Virwani, K.; Davis, B.; Cheng, J.Y.; Nelson, A. High-Throughput Directed Self-Assembly of Core-Shell Ferrimagnetic Nanoparticle Arrays. In *Langmuir*, **2013**, 29(24), 7472-7477.
- Van Blaaderen, A.; Rue, R.; Wiltzius, P. Template-directed colloidal crystallization. In *Nature (London)*, **1997**, 385(6614), 321-324.
- Meriguet, G.; Jardat, M.; Turq, P. Structural properties of charge-stabilized ferrofluids under a magnetic field: A Brownian dynamics study. In *J. Chem. Phys.*, **2004**, 121(12), 6078-6085.
- Meriguet, G.; Jardat, M.; Turq, P. Brownian dynamics investigation of magnetization and birefringence relaxations in ferrofluids. In *J. Chem. Phys.*, **2005**, 123(14), 144915/144911-144915/144918.
- Yamada, Y.; Enomoto, Y. Effects of oscillatory shear flow on chain-like cluster dynamics in ferrofluids without magnetic fields. In *Physica A*, **2008**, 387, 1-11.
- Eldin Wee Chuan Lim. Gelation of Magnetic Nanoparticles, Molecular Dynamics - Theoretical Developments and Applications in Nanotechnology and Energy, Prof. Lichang Wang (Ed.), ISBN: 978-953-51-0443-8, InTech, DOI: 10.5772/36155, **2012**.
- Xuan, Y.; Ye, M.; Li, Q. Mesoscale simulation of ferrofluid structure. In *Int. J. Heat Mass Trans.*, **2005**, 48, 2443-2451
- Davis, S.W.; McCausland, W.; McGahagan, H.C.; Tanaka, C.T.; Widom, M. Cluster-based Monte Carlo simulation of ferrofluids. In *Phys. Rev. E Stat. Phys., Plasmas, Fluids, Relat. Interdiscip. Top.*, **1999**, 59(2-B), 2424-2428.
- Richardi, J.; Pileni, M.P.; Weis, J.J. Self-organization of magnetic nanoparticles: A Monte Carlo study. In *Phys. Rev. E Stat., Nonlinear, Soft Matter Phys.*, **2008**, 77(6-1), 061510/061511-061510/061519.
- Huang, J.P.; Wang, Z.W.; Holm, C. Computer simulations of the structure of colloidal ferrofluids. In *Phys. Rev. E Stat., Nonlinear, Soft Matter Phys.*, **2005**, 71(6-1), 061203/061201-061203/061211.
- Duncan, P.D.; Camp, P.J. Aggregation Kinetics and the Nature of Phase Separation in Two-Dimensional Dipolar Fluids. In *Phys. Rev. Lett.*, **2006**, 97(10), 107202/107201-107202/107204.

36. Furlani, E.P. Analysis of particle transport in a magnetophoretic microsystem. In *J. Appl. Phys.*, **2006**, 99(2), 024912/024911-024912/024911.
37. Furlani, E.P.; Ng, K.C. Nanoscale magnetic biotransport with application to magnetofection. In *Phys. Rev. E Stat., Nonlinear, Soft Matter Phys.*, **2008**, 77(6-1), 061914/061911-061914/061918.
38. Nandy, K.; Chaudhuri, S.; Ganguly, R.; Puri, I.K. Analytical model for the magnetophoretic capture of magnetic microspheres in microfluidic devices. In *J. Magn. Magn. Mater.*, **2008**, 320(7), 1398-1405.
39. Henderson, J.; Shi, S.; Cakmaktepe, S.; Crawford, T.M. Pattern transfer nanomanufacturing using magnetic recording for programmed nanoparticle assembly. In *Nanotechnology*, **2012**, 23(18), 185304/185301-185304/185308.
40. Halverson, D.; Kalghatgi, S.; Yellen, B.; Friedman, G. Manipulation of nonmagnetic nanobeads in dilute ferrofluid. In *J. Appl. Phys.*, **2006**, 99(8, Pt. 3), 08P504/501-508P504/503.
41. Henderson, J.R.; Crawford, T.M. Repeatability of magnetic-field driven self-assembly of magnetic nanoparticles. In *J. Appl. Phys.*, **2011**, 109(7), 07D329/321-307D329/323.
42. Yellen, B.B.; Fridman, G.; Friedman, G. Ferrofluid lithography. In *Nanotechnology*, 2004, 15(10), S562-S565.
43. Yellen, B.B.; Friedman, G. Analysis of repulsive interactions in chains of superparamagnetic colloidal particles for magnetic template-based self-assembly. In *J. Appl. Phys.*, 2003, 93(10, Pt. 3), 8447-8449.
44. Yellen, B.B.; Friedman, G. Programmable Assembly of Colloidal Particles Using Magnetic Microwell Templates. In *Langmuir*, 2004, 20(7), 2553-2559.
45. Malik, V.; Petukhov, A.V.; He, L.; Yin, Y.; Schmidt, M. Colloidal Crystallization and Structural Changes in Suspensions of Silica/Magnetite Core-Shell Nanoparticles. In *Langmuir*, **2012**, 28(41), 14777-14783.
46. Furlani, E.P.; Ng, K.C. Analytical model of magnetic nanoparticle transport and capture in the microvasculature. In *Phys. Rev. E Stat., Nonlinear, Soft Matter Phys.*, **2006**, 73(6-1), 061919/061911-061919/061910.
47. Furlani, E.P.; Sahoo, Y.; Ng, K.C.; Wortman, J.C.; Monk, T.E. A model for predicting magnetic particle capture in a microfluidic bioseparator. In *Biomed. Microdevices*, **2007**, 9(4), 451-463.
48. Russel, W.B.; Saville, D.A.; Schowalter, W.R., *Colloidal Dispersions*, Cambridge University Press, **1989**.
49. Rosensweig, R.E. Fluid dynamics and science of magnetic liquids. In *Advances in Electronics and Electron Physics*. **1979**, Vol. 48: Martin M (ed.) Academic Press, New York, pp. 103-99
50. Beleggia, M.; Vokoun, D.; De Graef, M. Demagnetization factors for cylindrical shells and related shapes. In *J. Magn. Magn. Mater.*, **2009**, 321(9), 1306-1315.
51. Furlani, E.P. *Permanent Magnet and Electromechanical Devices; Materials, Analysis and Applications*. Academic Press, NY, **2001**.
52. Furlani, E.P.; Xue, X. A Model for Predicting Field-Directed Particle Transport in the Magnetofection Process. In *Pharm. Res.*, 2012, 29(5), 1366-1379.
53. Stratton, J.A. *Electromagnetic Theory*. New York: McGraw-Hill, **1941**.
54. Arfken, G. *Mathematical Methods for Physics*. 3rd ed. California: Academic Press, **1985**.
55. Furlani, E.P. A method for predicting the field in permanent magnet axial-field motors. In *IEEE Trans. Mag.*, **1992**, 28(5) 2061-2066.
56. Craik, D. *Magnetism: Principles and Applications*, John Wiley & Sons, **1995**, p 294-376.
57. Furlani, E.P. Computing the field in permanent magnet axial-field motors. In *IEEE Trans. Mag.*, **1994**, 30(5) 3660-3663.
58. Moon, F.C. *Magneto-solid Mechanics*, John Wiley & Sons, 1984.
59. Furlani, E.P. Field analysis and optimization of NdFeB axial field permanent magnet motors. In *IEEE Trans. Mag.*, **1997**, 33(5) 3883-3885.